iScience

CellPress
OPEN ACCESS

Article

A shape-deformable liquid-metal-filled magnetorheological plastomer sensor with a magnetic field "on-off" switch

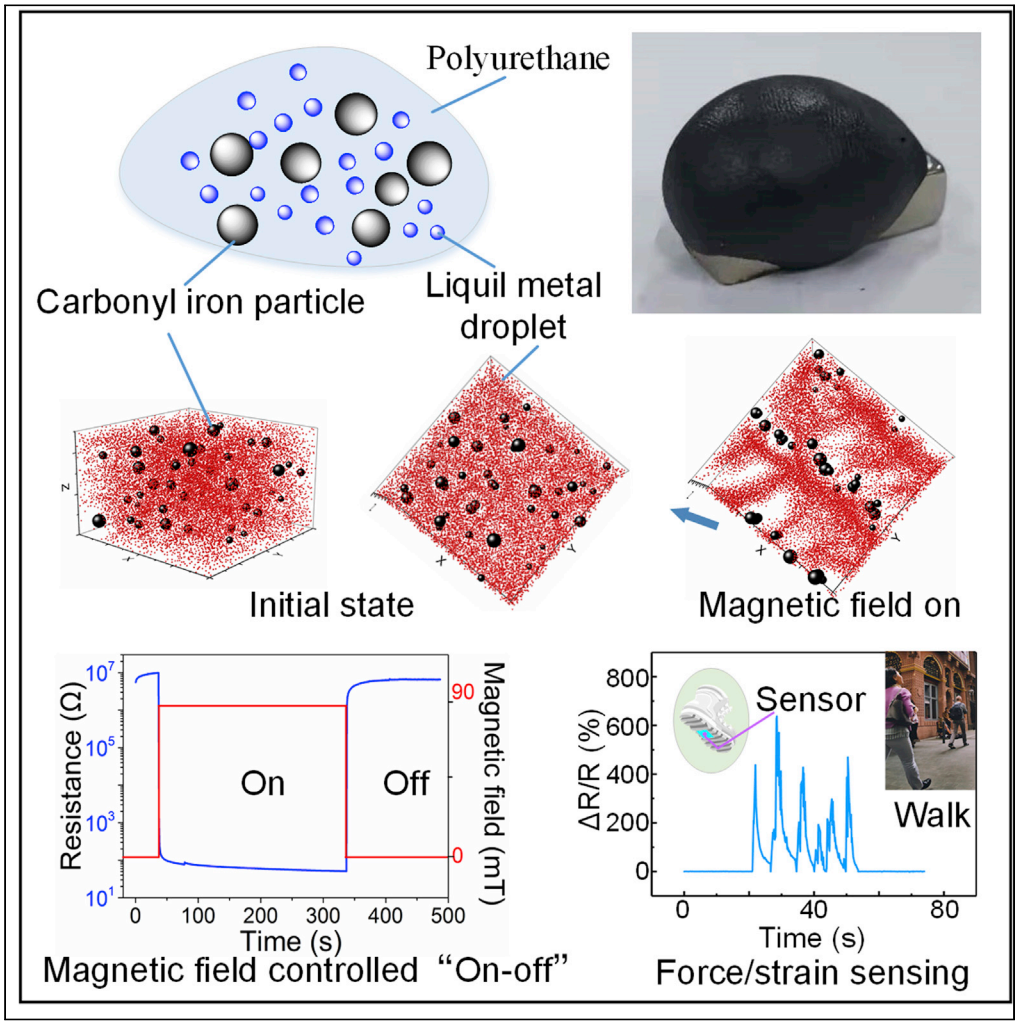

Jiaqi Xu, Haoming Pang, Xinglong Gong, Lei Pei, Shouhu Xuan

gongxl@ustc.edu.cn (X.G.)
xuansh@ustc.edu.cn (S.X.)

Highlights

A shape-deformable liquid-metal-filled magnetorheological plastomer was created.

The plastomer is sensitive to magnetic field, temperature, and force.

The evolution of the particle microstructure in the plastomer was simulated.

The plastomer has great potential in flexible electronics with magnetic control.

Xu et al., iScience *24*, 102549
June 25, 2021
https://doi.org/10.1016/j.isci.2021.102549

iScience

CellPress
OPEN ACCESS

Article

A shape-deformable liquid-metal-filled magnetorheological plastomer sensor with a magnetic field "on-off" switch

Jiaqi Xu,[1,3] Haoming Pang,[1,3] Xinglong Gong,[1,2,*] Lei Pei,[1] and Shouhu Xuan[1,2,4,*]

SUMMARY

Flexible viscoelastic sensors have gained significant attention in wearable devices owing to their exceptional strain-dependent electrical resistance. Most of the strain sensors are elastic composites, thus the internal stress is often preserved during the deformation when they are attached to the uneven target. Therefore, there is a pressing need for viscoelastic composites with highly self-adapted electromechanical properties sensitive to multiexternal circumstances. This work reports a liquid-metal-filled magnetorheological plastomer (LMMRP) that shows a high response behavior to the external stimulus such as magnetic field, temperature, and force. The shape-deformable LMMRP can transform from an insulator to a conductor under applying a magnetic field, thus the further viscoelastic sensor possesses a magnetic field "on-off" switch effect. The microstructure-dependent magnetic/thermal/mechanical-electrical coupling characteristics are investigated, and several proof-of-concept sensor applications, such as magnetic control, environment recognition, and motion monitoring, are demonstrated. These LMMRP composites show a broad potential in flexible sensors and soft electronics.

INTRODUCTION

With the rapid development of artificial intelligence, flexible sensors receive increasing attention in intelligent electronics, human-computer interaction, and biomedicine (Chen et al., 2018; Gao et al., 2020; Harada et al., 2014) because they can transduce multiple external stimuli (such as pressure, strain, light, and temperature) into electrical signals to mimic biological skin perception and satisfy complex working environments (Chen et al., 2017; Ha et al., 2018; Pyo et al., 2019; Yao and Zhu, 2014). Many efforts have been conducted on developing high-performance flexible sensors that can sensitively detect external physical stimuli. Unfortunately, the conductivity of these sensors usually degrades owing to the contact defects between the conducting components when encountered a large deformation or cyclic loading (Cheng et al., 2019; Jin et al., 2018). Besides, most of the flexible sensors comprise rigid conductive components dispersed within the elastic matrix, hence the microcrack often emerged when the aforementioned devices were installed on the uneven surface, which further limited the sensing applications (Yuan et al., 2019). Moreover, the elastic composites also exhibit undesirable shape deformation on the uneven surface (Ding et al., 2020). To this end, there is still a major challenge in manufacturing robust soft sensors for wearable electronics.

Different from the traditional flexible sensors, the viscoelastic composites that contain conductive fillers show enormous advantages such as shape-deformable, self-healing, and strain-adaptive properties (Wang et al., 2020; Xiong et al., 2020). Owing to the low matrix viscosity, the internal fillers form mobile networks, which can break and reform during mechanical deformation, and the final viscoelastic composites exhibit wonderful electromechanical behaviors (Kang et al., 2018; Lin et al., 2018). Boland et al. introduced the graphene into the viscoelastic Silly Putty matrices to develop a plastic sensor, using which the movement of a tiny spider can be detected (Boland et al., 2016). Interestingly, the electrical resistance showed a postdeformation temporal relaxation behavior and the resistivity was nonmonotonically changed with the strain owing to the freedom mobility of conductive fillers. Similarly, other adapted shapeable electronic devices with high sensing and self-healing performance can be achieved. Specifically, the viscoelastic sensors based on the shear thickening gel showed a quick sensitivity to the high energy impact or even bullet when

[1]CAS Key Laboratory of Mechanical Behavior and Design of Materials, Department of Modern Mechanics, CAS Center for Excellence in Complex System Mechanics, University of Science and Technology of China, Hefei 230027, PR China

[2]State Key Laboratory of Fire Science, University of Science and Technology of China, Hefei 230027, PR China

[3]These authors contributed equally

[4]Lead contact

*Correspondence: gongxl@ustc.edu.cn (X.G.), xuansh@ustc.edu.cn (S.X.)

https://doi.org/10.1016/j.isci.2021.102549

encountering an attack (Zhang et al., 2018; Zhao et al., 2019). Therefore, developing viscoelastic composites with unique reshapeable nature will be attractive in modern electronic devices.

The conductive microfillers/nanofillers including carbon nanotubes, silver nanowires, and graphene have been widely used in most flexible sensors (Amjadi et al., 2014; Kim et al., 2014; Qin et al., 2015). Composites with such fillers have low density, oxidation resistance, and good mechanical properties (Chand, 2000; Dresselhaus and Dresselhaus, 2002). However, the electrical resistance of these viscoelastic composites is often large which limited their broad applications. Recently, liquid metal (LM) has been intensively studied in the elastomer for its desired characteristics such as high electrical conductivity, thermal conductivity, and deformability (Dickey, 2017; Tang et al., 2016). The LM presents as microdroplets/nanodroplets in the polymer and deforms along with the external matrix (Kazem et al., 2018). Especially, Lin et al. report an extremely facile method to fabricate metallic wires with different geometries by stretching LM on polymeric substrates at room temperature (Lin et al., 2016). The wires show good electrical conductivity, and the diameters of the resulting wires can be as small as 10 μm. Because the mechanical and electric properties of composites can be simultaneously improved, many LM-based flexible electronics, including flexible electrodes, temperature sensors, and electronic circuits, have been developed (Gheribi and Chartrand, 2019; Guo et al., 2019; Ren et al., 2016, 2020; Yun et al., 2020). It has been reported that the LM can reduce the resistance of the flexible composites by forming conductive pathways between the hard inorganic conductive fillers (Wang et al., 2018). In consideration of its movability in a shape-deformable matrix, the LM microdroplets will be attractive in improving the electrical performance of the viscoelastic composites (Yun et al., 2019).

In addition, most previous sensors based on percolation conductive theory are always in the "turned-on" state, which inevitably meets the electric leakage and electric-thermal radiation. To solve this problem, a magnetic field switch is attractive because it remotely controls the conductive sensitivity to external strain or stress (Melzer et al., 2015). By imparting a magnetoresistive effect to artificial electronics, magnetic sensors are believed to open up new areas for intelligent electronic devices, including human health monitoring, intelligent control, and motion recognition (Kumar et al., 2018; Moulin et al., 2019; Wang et al., 2016). Unfortunately, magnetic particles are fixed in an elastic matrix after curing, reducing the sensitivity to magnetic fields (Zhang et al., 2019). At the same time, additional electromagnetic coils are needed to provide the magnetic field, and the lower sensitivity requires a higher magnetic field, which in turn spent more energy to maintain the magnetic field. Recently, a magneto-sensitive viscoelastic polymer consisting of low-cross-link-density polyurethane (PU) and magnetic particles, named magnetorheological plastomer (MRP), is developed. Under applying an external magnetic field, the magnetic particles can easily aggregate to form chain structures along the direction of the magnetic field, thereby the electromechanical coupling properties can be turned on or off (Xu et al., 2011, 2012, 2013). In this work, a 36-mT magnetic field is enough for the on-off switch control, and the power of the electromagnet is about 1W (1 V and 1 A). Moreover, the temperature and external force affect the microstructure of particle chains and endow MRP with temperature/force-sensitive performance (Pang et al., 2018; Xu et al., 2019). Therefore, viscoelastic composites with a magnetic field switchable piezoconductive property and shape-adaptive characteristics are desirable.

Here, this work reports a shape-deformable LM-filled magnetorheological plastomer (LMMRP) comprising LM microdroplets/nanodroplets, carbonyl iron (CI) microparticles, and viscoelastic PU with low cross-link density as the matrix. Under a magnetic field, the CI particles assemble into chain-like structures and contact with the LM microdroplets/nanodroplets to form conductive paths, making the material change from an insulator to a conductor, thus the sensor can be turned "on-off" by using a magnetic switch. Owing to simple preparation, fast response, and multiple functions, the LMMRP has become one of the attractive candidates for flexible sensors and soft electronics. The electrical characteristics of the LMMRP under different magnetic fields, temperatures, and forces are explored. Moreover, the magnetic/thermal/mechanical-electrical coupling mechanism is systematically analyzed and the microstructure of the particles is simulated by particle dynamic simulation methods. Finally, the LMMRP is demonstrated to have broad potential in smart electronics such as intelligent control, environmental monitoring, motion recognition, and so on.

RESULTS AND DISCUSSION

Preparation and characterization of the LMMRP with magnetic-field-controllable mechanical and electric behavior

Figure 1A illustrates the fabrication of LM-doped polyurethane (LMPU) and LMMRP. Briefly, 1 $mol \cdot L^{-1}$ NaOH-treated LM (EGaIn 75% gallium and 25% indium) and homemade PU were mixed in a beaker

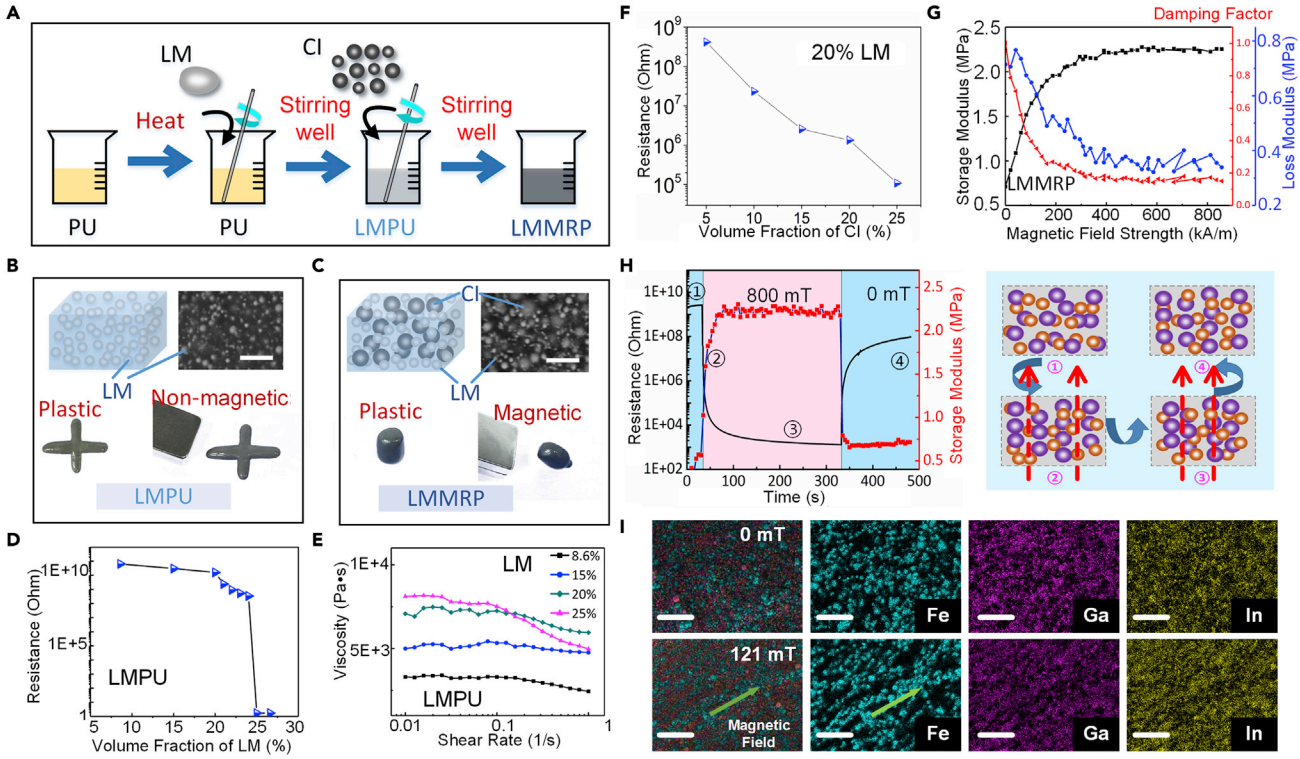

Figure 1. Fabrication and characterizations of liquid-metal-doped polyurethane (LMPU) and LMMRP

(A) Schematic diagram of the procedures for LMPU and LMMRP.

(B and C) Schematic diagrams, SEM images (scale bars are 6 μm), and photographs of LMPU (20%) and LMMRP (20% LM, 20% CI, big balls represent CI particles and small balls represent LM droplets). Compared with LMPU, the LMMRP can maintain its shape and be attracted by a magnet.

(D) Resistances of the LMPU doping with different contents of LM. Resistances are the average results of three tests.

(E) Viscosity curves of LMPUs with different LM contents in shear mode. During the test, a PP20 rotor is used. The distance between rotor and base is 1 mm and each data point is collected every 5 s.

(F) Resistance of the LMMRP doping with different contents of CI particles without a magnetic field. Resistances are the average results of three tests.

(G) Storage modulus/loss modulus/damping factor of the LMMRP (20% LM, 20% CI) under a varied magnetic field. The test frequency is 5 Hz and the strain amplitude is 0.1%.

(H) Resistance/storage modulus and schematic illustration of the microstructure of the LMMRP (20% LM, 20% CI) under an 800-mT magnetic field. The purple balls represent CI particles, the orange balls represent LM microdroplets/nanodroplets.

(I) Energy-dispersive X-ray spectroscopy element mappings of isotropic LMMRP (20% LM, 20% CI) and anisotropic LMMRP (20% LM, 20% CI). The LMMRP is placed in a 121 mT magnetic field for 5 min to obtain the anisotropic LMMRP (scale bars are 25 μm). All filler contents in the text refer to volume fraction. The viscosity and storage modulus of LMMRP are tested by a commercial rheometer and the resistance is tested by a ModuLab material test system.

See also Videos S1–S3.

with stirring thoroughly to prepare LMPU. Then, the CI particles were added into the LMPU by vigorous stirring and the LMMRP was obtained. The SEM image of LMPU (20% LM, all filler contents in the text refer to volume fraction) indicated that the LM was broken into microdroplets/nanodroplets of 100 nm–2 μm during mixing, and they were well distributed in the LMPU composite (Figure 1B). Clearly, the cross-shaped LMPU exhibited good plasticity and could be molded into various shapes. When a permanent magnet approached LMPU, it would not be attracted and deformed. Furthermore, its resistance was kept as a constant under a periodic magnetic field (see Figure S1). Then, the magnetic LMMRP was obtained by introducing CI particles into LMPU. Figure 1C shows the schematic formation and energy-dispersive X-ray spectroscopy (EDS) element mapping of the LMMRP (20% LM, 20% CI). CI particles (2–10 μm, the blue area is for Fe element) and LM microdroplets/nanodroplets (100 nm–2 μm, the pink area is for Ga element and the yellow area is for In element) were both well mixed and uniformly distributed in the PU matrix. The LMMRP was plastic and could be formed into a cylindrical shape as it did not yield under its own weight as the LMPU would. Here, the cylindrical LMMRP could be attracted by a permanent magnet to tilt and deform, which exhibited a typical magnetic sensitivity (see Video S1).

The electrical resistance of the LMPU filled with different volume fractions of LM was tested by a ModuLab material test system. As shown in Figure 1D, with the volume fraction of LM being increased from 8.6% to 20%, the resistance of the LMPU remained greater than 10^{10} Ω. In the range of 20%–24%, the resistance of LMPU decreased from 1.6×10^{10} Ω to 3.4×10^{8} Ω. Once the volume fraction changed to 25%, there was a sharp decline by more than 8 orders and the resistance remained at 1.6 Ω when the volume fraction continued to increase. Obviously, starting from 20%, the filler content had a significant effect on the sample resistance. Different from traditional electronic sensors, the sensitivity of the LMMRP depended greatly on the magnetic field. To ensure the high sensitivity and controllability of the sample to the magnetic field, the optimal volume fraction of LM was determined to be 20%.

Furthermore, Figure 1E shows the viscosity of the LMPU with different LM contents and the viscosity increased with the increasing volume fraction of the LM. The viscosity of LM and PU was about 7 Pa and 8000 Pa, respectively. Here, the LM was uniformly dispersed in PU in the form of microdroplets/nanodroplets. Owing to the large surface tension, it was very difficult for LM droplets to flow. So, the viscosity of LMPU increased with the increasing volume fraction of the LM. However, when the LM in LMPU reached 25%, the initial viscosity also increased with an increasing volume fraction of LM, but its viscosity decreased with increasing shear rate. Because the resistance of LMPU with 25% LM was very small, the micro/nano-LM droplets in PU were densely packed. With the increase of shear rate, some microdroplets/nanodroplets connected with each other to large droplets or even lines during the test process (see Figure S2). The convergence of LM droplets enhanced the flowability of LMPU, resulting in a decrease of viscosity.

Based on the aforementioned analysis, the optimal volume fraction of LM in LMPU was determined to be 20%. As for the LMMRP, adding of CI particles would also affect its conductivity. So, LMMRPs with 20% LM and different content of CI particles were prepared and their resistances were tested. As shown in Figure 1F, the resistance decreased with the increasing volume fraction of CI particles. To achieve a good switching effect, it is necessary to increase the content of iron powder as much as possible on the premise of ensuring the softness of the sample. The experimental results show that 20% is the best volume fraction of CI particles, and the viscosity of the sample will increase sharply with the further increase of CI content (Figure S3). So, the LMMRP with 20% LM and 20% CI content was prepared as a representative sample with good flexibility and magnetic field "on-off" switch effect. It is worth noting that for the LMMRP with 20% LM and 20% CI content, the rest volume for LM distribution becomes denser owing to the addition of CI, and the volume fraction of LM in the PU is 25%, but the resistance of LMMRPs (10^{5} Ω) is greater than that of LMPU with 25% LM (1 Ω). So, the addition of CI particles is beneficial to the dispersion of LM and hinders aggregation of LM (see Figure S4). The magnetorheological effect is the ratio of magnetic-induced storage modulus to initial storage modulus and the magnetic-induced storage modulus is the storage modulus under a magnetic field minus the initial storage modulus. Here, the LMMRP with 20% LM and 20% CI content was prepared as a representative sample with typical mechanical and electrical properties. The storage modulus of the LMMRP (20% LM, 20% CI) increased with an increasing magnetic field, and the magnetorheological effect could reach 300% (Figure 1G). Under applying the magnetic field, the CI particles dispersed in the matrix were aggregated into chain-like structures, which not only improved the mechanical properties but also facilitated the formation of conductive paths with the LM microdroplets/nanodroplets to improve the electrical conductivity of the sample.

Figure 1H shows the resistance and storage modulus of the LMMRP (20% LM, 20% CI) under an 800-mT magnetic field. Initially, the CI and LM droplets were evenly distributed in the composite. The initial distance between the particles was large and the resistance of LMMRP was greater than 10^{9} Ω. When a magnetic field was applied, the CI particles aggregated into chain structures along the direction of the magnetic field, which increased the storage modulus. At the same time, during the aggregation of magnetic particles, the LM droplets were pushed by CI particles and dispersed between CI particles chains. LM droplets pushed by CI particles were also arranged along the CI particle chains, which was equivalent to increasing the volume fraction of LM along the direction of the magnetic field, thus the resistance was reduced. When the particles formed a stable structure, the changes in storage modulus and resistance of the LMMRP tended to be gentle. Once the magnetic field was removed, the magnetic dipole force between the CI particles disappeared, and the distance between CI particles increased to reduce the total potential energy. The soft PU polymer quickly encapsulated the CI and LM droplets, broke the conductive path, and increased the resistance. However, owing to the plastic matrix, the CI particles cannot return to the initial position, so the storage modulus was larger than that in the initial state, and the resistance was smaller than the initial resistance.

To demonstrate the magnetically dependent microstructure evolution of the LMMRP, the distribution of CI and LM was analyzed by EDS for mapping their characteristic elements (Figure 1I). The CI particles and LM droplets were evenly distributed in the LMMRP without a magnetic field. When a 121-mT magnetic field was applied, the CI particles aggregated into chain structures parallel to the direction of the magnetic field (the green arrow). The position of LM droplets filled around the CI particle also changed with the movement of CI particles. Importantly, the microstructure evolution in response to the magnetic field had a significant impact on the mechanical and electrical properties of the LMMRP. In this work, it is found that the shape-deformable LMMRP (20% LM, 20% CI) can transform from an insulator to a conductor under applying a magnetic field. Without the magnetic field, the LMMRP shows few responses to the external forces. As a result, the viscoelastic sensor based on the LMMRP possessed a magnetic field "on-off" switch effect, which must be originated from the movable chain-like structures along the direction of the magnetic field.

Magnetic-electrical sensing properties of the LMMRP with the magnetic field "on-off" switch effect

To further study the magnetically dependent electrical properties, the electrical responses of the LMMRP under different magnetic field was conducted. Figure 2A shows the experimental equipment, which consists of an electrical property test system (ModuLab MTS), a commercial rheometer with electromagnetic equipment (Physica MCR301), and a preprogrammed control and data storage system. The LMMRP with a diameter of 20 mm and a thickness of 1 mm was placed between the rotor and base of the rheometer, which was covered with conductive copper foils as the electrodes by the insulating gel. The distance of two electrodes can be controlled, and the normal force of the sample is collected. The equipped electromagnet supplied a uniform magnetic field from 0 to 800 mT. The ModuLab MTS measured the electrical resistance and current of the sample by outputting a DC voltage. Ultimately, the mechanical and electrical data were stored in the data storage system.

Figure 2B shows the curves of the magnetic flux density/normal force/resistance of the LMMRP (20% LM, 20% CI) response to time. The periodic magnetic fields were set as 90 mT, 180 mT, 360 mT, 540 mT, and 720 mT. Correspondingly, the peak values of normal force and electrical resistance increased periodically from 1.5 N to 18.8 N and decreased periodically from 87,403 Ω to 497 Ω, respectively. Under the magnetic field, the magnetic dipole force between the CI particles attracted each other to form a chain structure along the magnetic field. As the magnetic field increased, the magnetism-induced force increased, and the CI particles were tightly aggregated. Moreover, some CI particles broke through the PU matrix shell and directly contacted together to form a cluster structure, resulting in an increase of the normal force and the conductivity. In addition, the LM droplets were pushed by CI particles and aggregated around the CI particle chains. To demonstrate this, a similar experiment was performed and shown in Videos S2 and S3. In Video S2, a steel ball with 1.6 mm in diameter was used. LM droplets were irregular in shape and were smaller than the steel ball. The steel ball was attracted by a magnet and could be moved in PU. LM droplets were pushed by the steel ball and moved together with the steel ball. Here, different from other polymer matrices, LM droplets and CI particles in LMMRP were well encapsulated by PU, while they only aggregated but did not fuse (Markvicka et al., 2018; Park et al., 2019). In Video S3, the steel ball was attracted in the opposite direction, and the LM droplets were separated from each other. In a word, the CI particles formed a chain-like structure under the action of the magnetic field and formed a conductive path together with the surrounding LM droplets to reduce the resistance of the composites.

Figures 2C and 2D illustrate the influence of CI and LM content on the magnetic-field-dependent conductivity of the LMMRP. Obviously, when the CI and LM content increased from 5% to 25% and 20% respectively, the peak of the electrical current increased by 6 orders of magnitude. More CI particles not only increased the chain numbers but also led the chain structures to be denser and thicker, thus conductive paths increased and the resistance reduced. In this case, the LM affected the LMMRP by improving both the conductivity of the PU matrix and the CI chain conductive path. The magnetization curves and viscosities of the LMMRP with different CI and LM contents are shown in Figure S3. When the CI content was 25%, the viscosity decreased with increasing shear rate, which may be caused by the fusion of some LM droplets into larger droplets. At the same time, CI increased the stiffness of LMMRP *via* the typical particle-strengthening effect, which harmed the softness and comfort of the sample. Therefore, the filler contents of LM and CI were kept at 20% as the optimum condition.

The relative resistance variation $\Delta R/R$ ($\Delta R = R'-R$, R' was the real-time resistance and R was the initial resistance) at the different magnetic flux density was shown in Figure 2E. The magnetic field sensitivity coefficient (GF_m), the ratio of the absolute value of relative resistance variation to the magnetic flux density

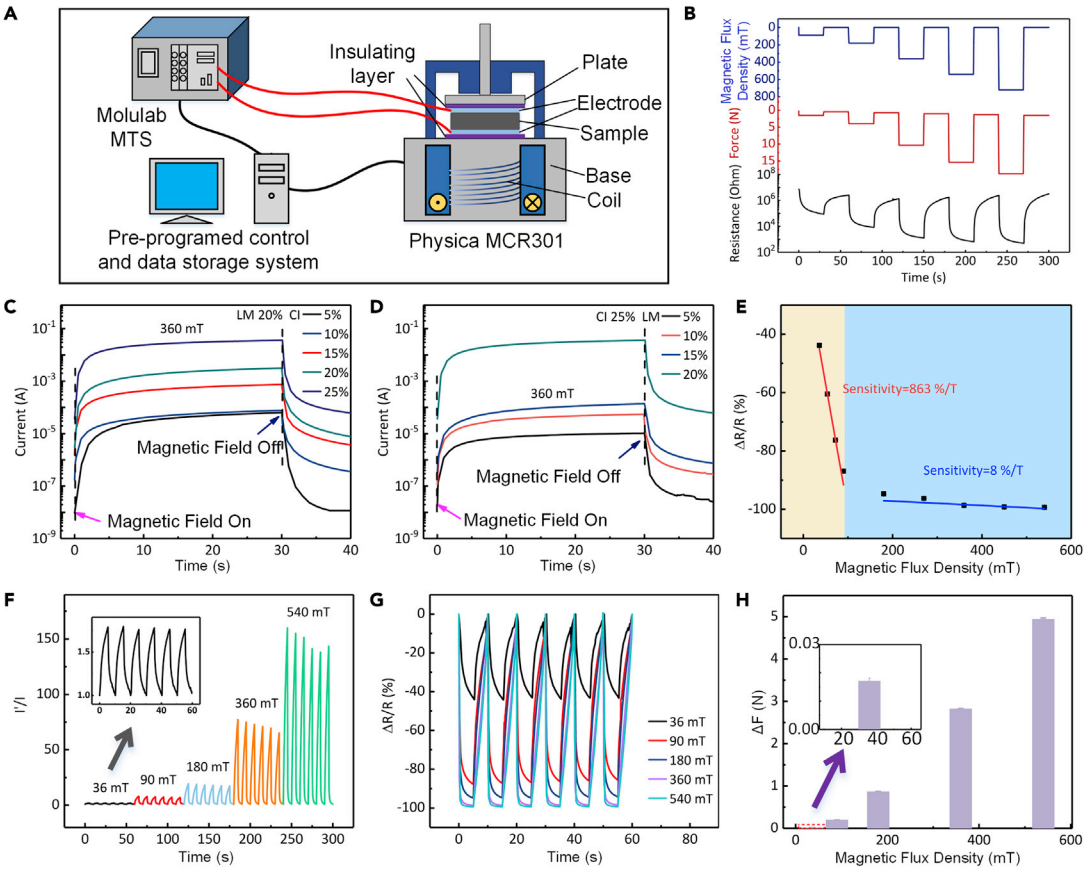

Figure 2. Electrical responses of the LMMRP to the magnetic field

(A) Schematic illustration of measurement system for the magnetic sensing test.

(B) Real-time response of the resistance, force, and magnetic flux density.

(C) The sensing performance of the LMMRP with different CI contents under a 360-mT magnetic field.

(D) The sensing performance of the LMMRP with different LM contents under a 360-mT magnetic field.

(E) Relative resistance variation of the LMMRP (20% LM, 20% CI) under various magnetic fields. Resistances are the average results of three tests.

(F) Real-time response of the current in the LMMRP (20% LM, 20% CI) at different magnetic field cyclic tests.

(G) Real-time resistance response of the LMMRP (20% LM, 20% CI) at different magnetic field cyclic tests.

(H) Force changes of the LMMRP (20% LM, 20% CI) in the magnetic field. Forces are the average results of three tests. Data represented as mean ± standard error of the mean.

change, was used to characterize the magnetic response sensitivity. In two magnetic flux density ranges of 36 mT–90 mT and 180 mT–540 mT, the sensitivity coefficients were 863%/T and 8%/T, respectively. Under a small magnetic field, the magnetic dipole forces on some CI particles were smaller than the yield stress of the matrix, and these particles would not move. With the increase of the magnetic field, magnetic dipole forces increased and the particle structure changed continuously. When the magnetic field was larger than 100 mT, the internal particle structure of the LMMRP tended to be stable. As the magnetic field further increased, the internal structure changed little, so the magnetic field sensitivity coefficient under a high magnetic field was much lower than that under a low magnetic field. Moreover, the absolute ΔR/R can reach more than 95%, which reflected the excellent sensitivity to the magnetic field. Figures 2F and 2G exhibit a stable and repeatable electrical response under multiple continued cyclic magnetic fields, which means that the LMMRP has a good potential application in the magnetic sensing field. The ordinate in Figure 2F is the normalized current I'/I, where I' represents the real-time current and I represents the initial current. During the experiment process, the change of normal force also increased with the magnetic field (Figure 2H), which reflected the enhancement of the magnetic field-induced CI particle chains.

The electrical resistance of LMMRP could be changed by several orders of magnitude owing to the adjustment of the magnetic field. Therefore, the sensor based on the LMMRP was adopted in a

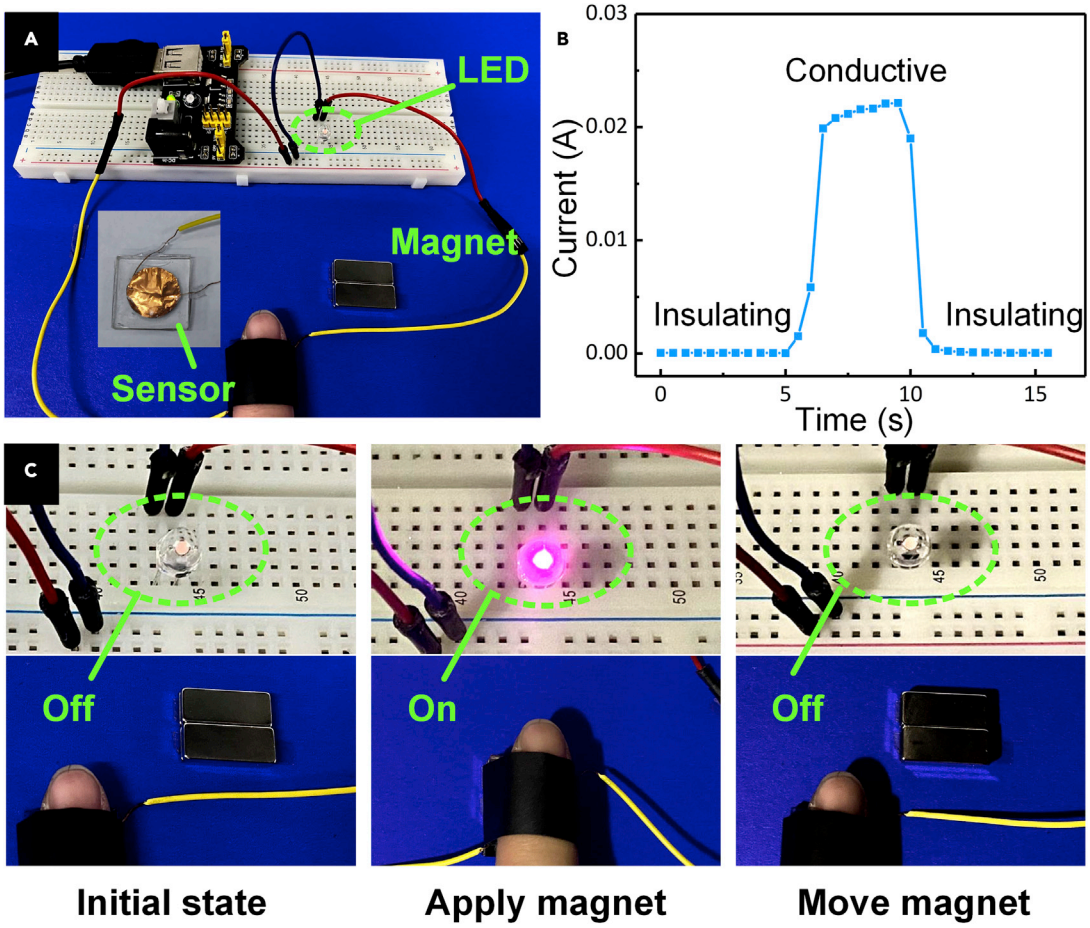

Figure 3. Application of the LMMRP in a magneto-controlled switch

(A) Digital images of the sensor and the magneto-controlled circuit device.

(B) The current in the magneto-controlled circuit.

(C) Demonstration of a magneto-controlled bulb turning on or off.

See also Videos S4.

magneto-controlled switch (Figure 3A). The sensor consisted of a PDMS shell, an LMMRP, and two copper foils. A cylindrical LMMRP (Φ20 × 1 mm) with two copper foils pasted on the upper and lower surfaces of the MRP was wrapped by a PDMS shell (30 mm × 30 mm × 2 mm). During the test, a copper wire was connected to each copper foil to transmit electrical characteristics. As shown in Figure 3C, the LMMRP coated with PDMS was fixed on the finger and connected to the circuit. When a finger approached the magnet, the resistance dropped so that the bulb lighted up. However, the bulb was immediately turned off as soon as the finger was removed from the magnet (see Video S4). The current in the magneto-controlled circuit is shown in Figure 3B. Magnetic sensitivity and electrical controllability make LMMRP perform well in intelligent electronic devices.

Thermal-magnetic-electrical coupling properties of the LMMRP

Interestingly, the electrical property of LMMRP is also sensitive to temperature. Figure 4A illustrates the real-time relative resistance variation ΔR/R at different temperatures under a square wave of the magnetic field with an amplitude of 36 mT. The peak value of the absolute ΔR/R changed from 43% to 77% as the temperature increased from 25°C to 70°C. The PU matrix was a soft polymer whose viscosity decreased with increasing temperature because of the unwinding of molecular chains at high temperatures (Chen, 2013) (Figure 4C). The viscosity of the matrix harmed the formation of CI particle chains. In a low-viscosity matrix, CI particles could quickly form dense and thick chain-like structures that combined with LM droplets as the conductive paths. This macroscopic performance is proven by the increasing phenomenon of normal

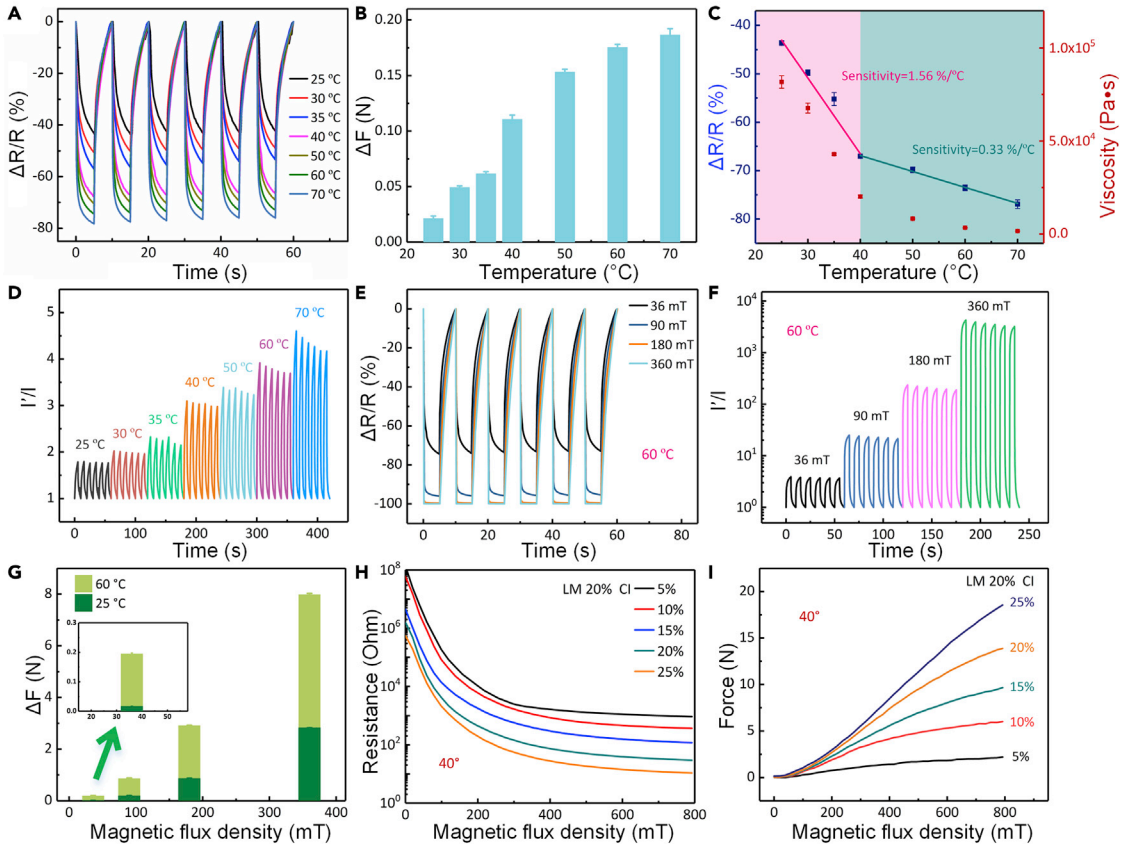

Figure 4. Thermal sensing performance of the LMMRP

(A) Relative resistance variation ΔR/R of the LMMRP (20% LM, 20% CI) at different temperatures under the square wave of the magnetic field with an amplitude of 36 mT.

(B) The change of normal force in the process of magnetic field switching under different temperatures. The variation amplitude of the magnetic field is 36 mT. Forces are the average results of three tests. Data represented as mean ± standard error of the mean.

(C) Minimum relative resistance variation ΔR/R of the LMMRP (20% LM, 20% CI) and viscosity of PU matrix in various temperatures. Resistances are the average results of three tests. Data represented as mean ± standard error of the mean.

(D) The real-time current in the LMMRP (20% LM, 20% CI) under different temperatures and the triangular wave of the magnetic field with an amplitude of 36 mT.

(E) Relative resistance variation ΔR/R of the LMMRP under the square wave of the magnetic field with different amplitude at 60°C.

(F) The real-time current in the LMMRP under the triangular wave of the magnetic field with different amplitude.

(G) The change of normal force in the process of magnetic field switching with different amplitudes at 25°C and 60°C. Forces are the average results of three tests. Data represented as mean ± standard error of the mean.

(H and I) Resistance and normal force of the LMMRP with different CI contents in a varied magnetic field.

force (Figure 4B) and electrical conductivity when a magnetic field is applied on the LMMRP (Figures 4A, 4C, and 4D). Here, the normal force was originated from the formation of CI chains under the action of the magnetic field. The magnetic particles would move along the direction of the magnetic field, leading to an expanded force. With increasing the temperature, the PU matrix became soft and the binding effect on CI particles decreased, which led to a more compact particle structure. Therefore, the normal force increased with the increasing temperature. We also defined the ratio of the absolute relative resistance variation to the temperature change as the temperature sensitivity coefficient (GF_t) to describe the temperature-dependent conductivity (Figure 4C). The ΔR/R was measured after applying the magnetic field for 60 s to ensure that the resistance was stable (Pang et al., 2015). After calculation, GF_t was approximated 1.56%/°C in the range of 25°C–40°C and 0.33%/°C in the range of 40°C–70°C, by a linear fitting method. The viscosity also presented a synchronous change trend in the two regions, which further confirmed that the viscosity affected the magnetism-induced microstructure evolution and magnetic-field-dependent conductivity.

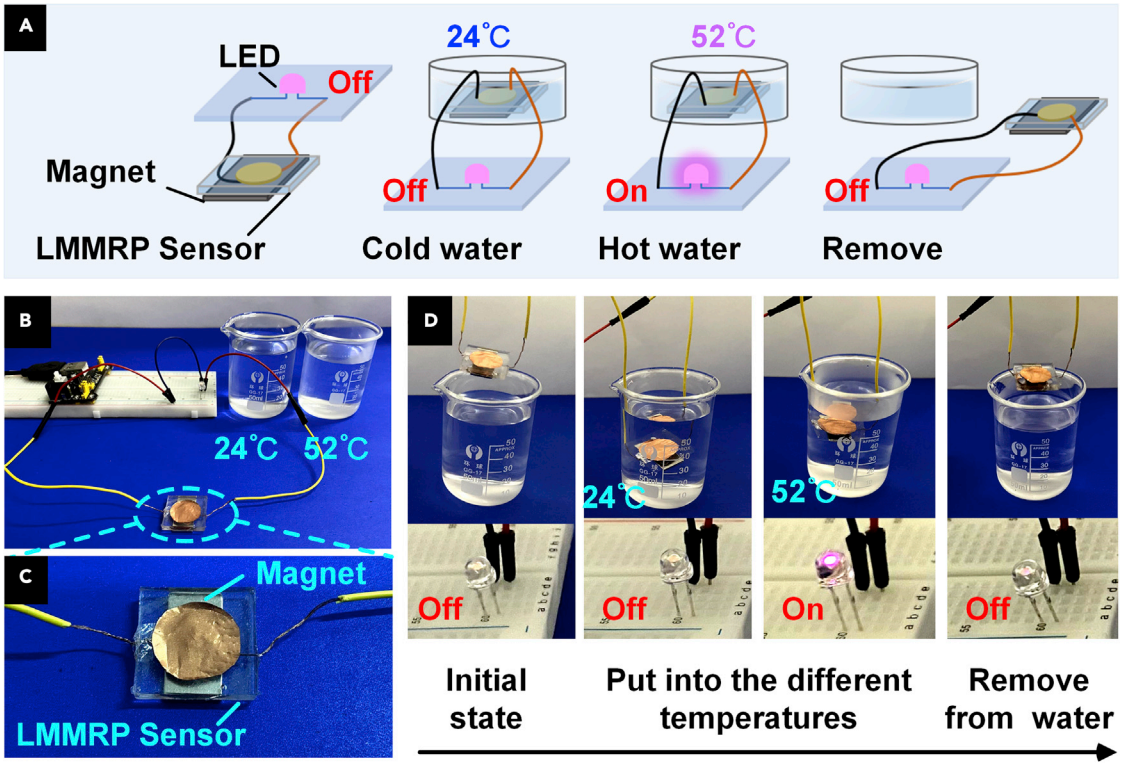

Figure 5. Temperature sensing behavior and monitoring device of the LMMRP

(A–C) Schematic diagram digital image of the LMMRP temperature monitoring device. (A) Schematic diagram. (B) Digital image of the LMMRP temperature monitoring device. (C) The LMMRP temperature sensor.

(D) Demonstration of an LMMRP temperature sensor sinking in water at different temperatures.

See also Videos S5.

The electrical response to different multiple periodic magnetic fields at the high temperature is presented in Figures 4E and 4F. When the magnetic field was set as 180 mT and 360 mT, the peak value of the relative resistance variation $\Delta R/R$ was −99.5% and −99.97%, and the normalized current I'/I changed by 2 and 3 orders of magnitude, respectively. Excellent and repeatable electrical response at high temperature meant that the LMMRP showed wonderful magnetic control and magnetic sensing performance which would be applied in complex conditions. Figure 4G is a comparison of the normal force variation at 25°C and 60°C. Notably, the normal force variation increased with the magnetic flux density, and it was higher at 60°C than that at 25°C. In addition, the resistance and normal force change of the LMMRP with different CI contents at 40°C under magnetic field are investigated (Figures 4H and 4I). Under a magnetic field, the chain-like conductive paths combined by CI particles became denser and thicker as the CI content increased, resulting in smaller resistance and larger normal force change.

The difference in electrical performance of the LMMRP at different temperatures is beneficial for the sensor to detect and identify the environment temperature. Figures 5A and 5B show the schematic diagram of the temperature-sensing behavior and the digital image of the LMMRP temperature-monitoring device. The sensor is composed of electrodes, LMMRP, wires, and PDMS, as described in the experimental section. A permanent magnet was placed at the bottom of the sensor to provide a 52-mT magnetic field (Figure 5C). It can be seen from Figure 5D that the bulb was always kept off when the sensor was placed in normal temperature water. Interestingly, once the sensor was placed in hot water, the bulb lighted up and then went off after the sensor was taken out of the water (see Video S5). In hot water, the matrix viscosity of LMMRP decreased and CI particles aggregated into a dense cluster-like structure under a small magnetic field. In combination with LM droplets, a conductive path with excellent conductivity was formed. The resistance of the LMMRP drastically decreased causing the current in the circuit to increase and the bulb to be turned on. In particular, the LMMRP has broad application prospects in temperature alarm devices and monitoring systems owing to its temperature-sensitive magnetoresistive characteristics.

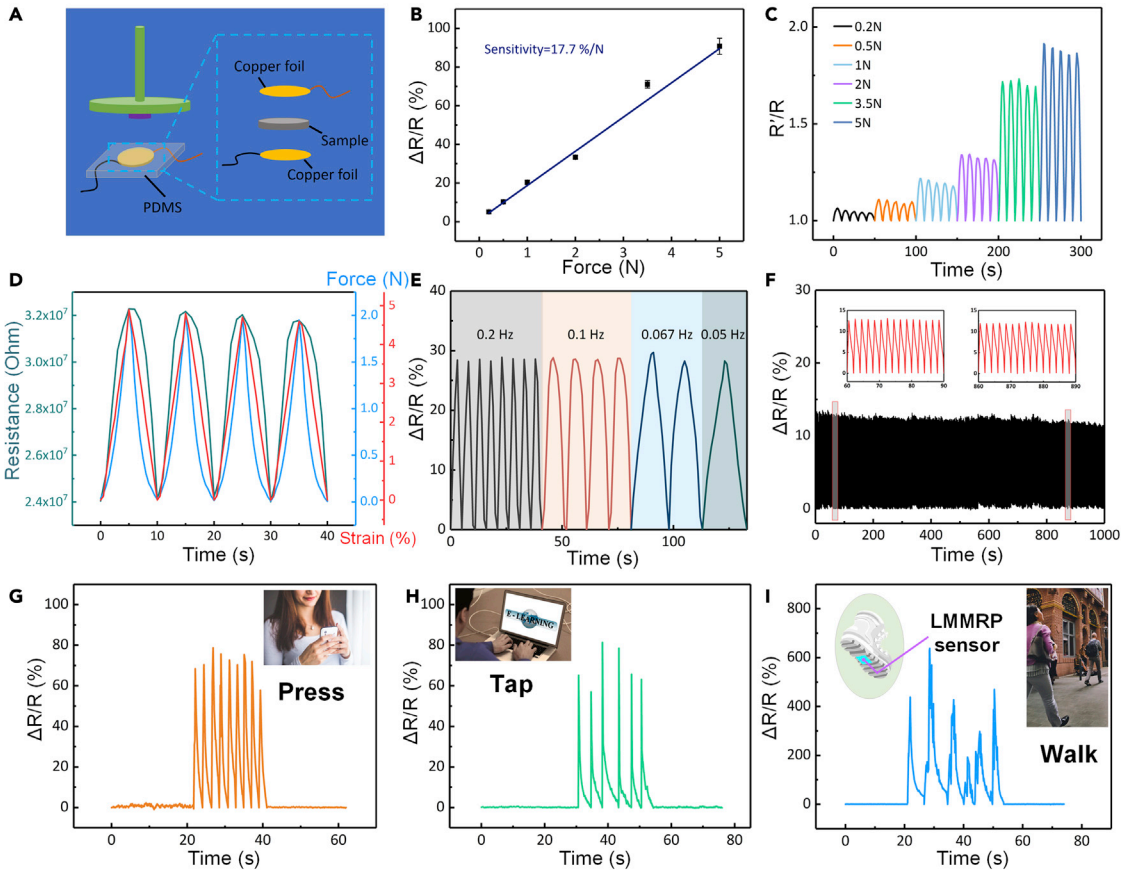

Figure 6. Force-sensing properties of the LMMRP (20% LM, 20% CI) sensor

(A) Schematic of the experimental setup for force sensing test. During the test, the upper plate moves downward to compress the sensor, the resistance and normal force are recorded.

(B) The relative resistance variation ΔR/R increased under different normal forces. Resistances are the average results of three tests. Data represented as mean ± standard error of the mean.

(C) Normalized resistance R′/R under triangular force wave with different amplitudes. R′ is the real-time resistance, and R is the initial resistance.

(D) Resistance/force/strain variation as a function of time.

(E) Relative resistance variation of the LMMRP sensor under triangular force wave with the frequency range from 0.05 to 0.2 Hz.

(F) Stability and robustness of the LMMRP sensor at a frequency of 0.5 Hz.

(G–I) Force perception behavior by finger press, tap, and human walk.

Mechanical-magnetic-electrical coupling performance of the LMMRP

In addition to being sensitive to magnetic field and temperature, the LMMRP can also feedback force behavior through an electrical signal. LMMRP is placed between two copper foil electrodes and encapsulated with PDMS, which improves the recoverable performance of the sample and prevents leakage during compression testing (Figure 6A). The rheometer accurately controls and simultaneously records compression force and displacement signals. In addition, the electromagnet device in the base of the rheometer provides a 35-mT uniform magnetic field in the force-sensing experiment. The relative resistance variation ΔR/R increased linearly with increasing force, and the sensitivity coefficient GF_f (the ratio of the relative resistance variation to the force change) was 17.7%/N (Figure 6B). As shown in Figure 6C, the normalized resistance R′/R (R′ is the real-time resistance and R is the initial resistance) produces a stable and repeatable response under a triangular force wave with different amplitudes. Furthermore, the consistency of electrical resistance, force, and displacement is revealed in Figure 6D. The self-assembled CI-LM chain-like conductive path was destroyed by sudden force, causing a rise in electrical resistance. Once the force was removed, the CI particles were reconstructed into a chain structure under the magnetic field so that the resistance decreased. Figure 6E illustrates that the frequency of force does not affect electrical performance. The multiple cyclic loading test demonstrates the LMMRP possesses good recoverability, reliability, and stability, which exhibits an outstanding application in continuous dynamic detection (Figure 6F).

Today, force sensors are closely related to people's work and life. The LMMRP sensor can also significantly respond to the finger pressing on the phone and tapping on the computer, implying its excellent detection sensitivity (Figures 6G and 6H). Moreover, the sensor tied to the sole can feedback the signal of walking to detect human activity (Figure 6I). Remarkable force sensing performance makes the LMMRP play an important role in an intelligent electronic device and human health monitoring. However, most of the previously reported force sensors based on percolation conductive theory are always "turned on," which inevitably meets the electric leakage and electric-thermal radiation owing to the conductive network in the sensor (Hu et al., 2020). Here, the present LMMRP with the magnetic field "on-off" switch effect successfully solved this problem, and the sensor can be intelligently controlled to the on or off state by attaching a small magnet.

Mechanism explanation and simulation of the LMMRP with the magnetic field "on-off" switch effect

Figures 7A–7D shows the schematic diagram of the microstructure affected by the magnetic field, temperature, and force. The evolution of particle microstructure in the LMMRP was also simulated by particle dynamics method to help understanding the magnetic/thermal/mechanical-electrical response mechanism. In the calculation process, the force between the particles (CI particles and LM droplets) and the force between the particles and the matrix are considered. The magnetic moment vector $\boldsymbol{m}_i$ of a CI particle i in a uniform magnetic field $\boldsymbol{H}$ can be determined by the following exponential formula:

$$\boldsymbol{m}_i = MV_i\frac{\boldsymbol{H}}{H} = M_S\left(1-e^{-\chi H}\right)V_i\frac{\boldsymbol{H}}{H} \qquad \text{(Equation 1)}$$

Here, M is the magnetization of the CI particle. $V_i = \pi {d_i}^3/6$ is the volume of the particle i, and d_i is the diameter of the particle i. $\chi = 4.91 \times 10^{-6}$ m/A is a constant. CI Particle i is magnetized in the magnetic field, generating a new magnetic field:

$$\boldsymbol{H}_i = -\frac{1}{4\pi r^3}\left[\boldsymbol{m}_i - 3(\boldsymbol{m}_i \cdot \hat{\boldsymbol{r}})\hat{\boldsymbol{r}}\right] \qquad \text{(Equation 2)}$$

where r is the position vector from the particle i to a position point, $\hat{\boldsymbol{r}} = \boldsymbol{r}/r$. Therefore, the magnetic moment of a particle in a magnetic field should be expressed as

$$\boldsymbol{m}_i = M_S\left(1-e^{-\chi H_l}\right)V_i\frac{\boldsymbol{H}_l}{H_l},\ \boldsymbol{H}_l = \boldsymbol{H} + \sum_{j\neq i}\boldsymbol{H}_j \qquad \text{(Equation 3)}$$

In summary, the magnetic dipole force of the particle i generates by the particle j is

$$\boldsymbol{F}_{ij}^{m} = \frac{3\mu_0}{4\pi {r_{ij}}^4}c_m\left[\left(-\boldsymbol{m}_i\cdot\boldsymbol{m}_j + 5\boldsymbol{m}_i\cdot\boldsymbol{t}\boldsymbol{m}_j\cdot\boldsymbol{t}\right)\boldsymbol{t} - (\boldsymbol{m}_i\cdot\boldsymbol{t})\boldsymbol{m}_j - \left(\boldsymbol{m}_j\cdot\boldsymbol{t}\right)\boldsymbol{m}_i\right] \qquad \text{(Equation 4)}$$

where r_{ij} represents the distance between two CI particles. μ_0 is the magnetic permeability of the matrix. $\boldsymbol{t}$ is the unit vector pointing from particle i to particle j. c_m is the correction factor of the point dipole model (Keaveny and Maxey, 2008). The specific expression of c_m and the CI particle size distribution can refer to the literature source (Liu et al., 2013a). For LM droplets, $\boldsymbol{m}_i = 0$. To simplify the calculation, it is assumed that the droplet was a sphere with a diameter of 1 μm. In addition to magnetic dipole force, van der Waals force $\boldsymbol{F}_{ij}^{vdW}$ also exists between two particles (Pei et al., 2019):

$$F_{ij}^{vdW} = \frac{8A}{3}L_{ij}d_id_j\left[\frac{1}{4L_{ij}^2-\left(d_i+d_j\right)^2}-\frac{1}{4L_{ij}^2-\left(d_i-d_j\right)^2}\right]^2\boldsymbol{t} \qquad \text{(Equation 5)}$$

Here, $A = 5 \times 10^{-19}$ was the Hamaker constant of the particles. $L_{ij} = max[r_{ij},\ d_{ij} + h_{min}]$, $h_{min} = 0.001d_{ij}$ (Klingenberg et al., 2010). To prevent particles from overlapping, a repulsive force $\boldsymbol{F}_{ij}^{r}$ is also introduced:

$$\boldsymbol{F}_{ij}^{r} = -\frac{3\mu_0 m_{si}m_{sj}}{2\pi d_{ij}^4}10^{-10\left(\frac{r_{ij}}{d_{ij}}-1\right)}\boldsymbol{t} \qquad \text{(Equation 6)}$$

Here, m_{si} and m_{sj} are the saturation magnetization of the target particles. As for LM droplets, when two droplets were close to each other, the droplet fusion needed to overcome the limitation of the matrix. Owing to the high viscosity of the PU ($\eta = 8000$), we assumed that the droplets would not fuse and a polyurethane film was presented between the droplets (see Videos S2 and S3). The deformation of LM droplets

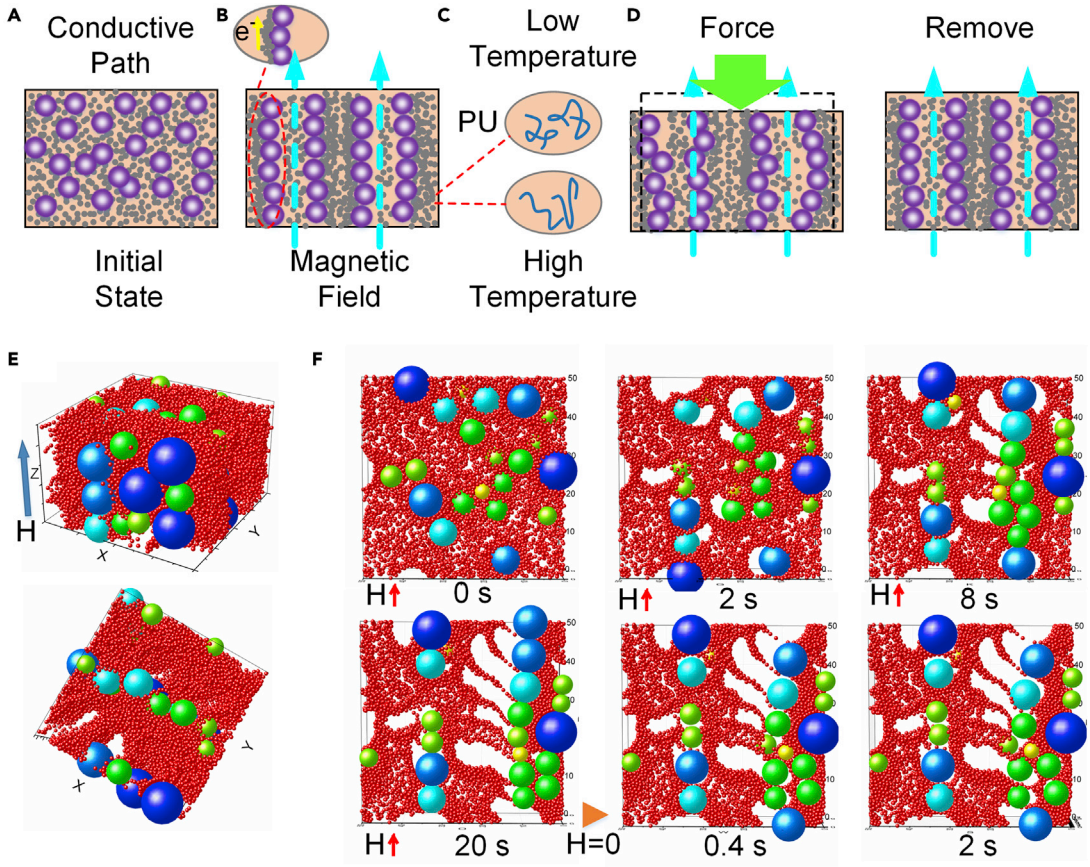

Figure 7. Schematic diagram of microstructure evolution and microstructure simulation of the LMMRP

(A–D) Schematic diagram of the microstructure evolution of the LMMRP under different stimulations (A) Initial state. (B) Applying a magnetic field. (C) Under different temperatures. (D) Under stress. Purple balls represent CI particles and gray balls represent LM droplets.

(E) Perspective view and top view of simulated microstructures in the LMMRP by particle dynamics methods. The blue and green balls represent CI particles and red balls represent LM droplets.

(F) The evolution of microstructures in LMMRP in a 5-μm-thick rectangular area. A 560 kA/m magnetic field was applied in the first 20 s, then the magnetic field was removed.

was also ignored to simplify the simulation. Therefore, the magnetization of the LM droplet $m_{si} = MV_i$, when calculating the repulsive force.

Particle-matrix interaction includes drag force and buoyancy. Here, Brownian motion is ignored. The PU matrix is incompressible and approximately regarded as Bingham fluid. The motion of particles has an extremely low Reynolds number. Hence, the hydrodynamic drag force is given by the following equation:

$$F_i^d = -\frac{19}{8}\pi\left(\tau_0 d_i^2 \hat{\mathbf{v}} + d_i \eta \mathbf{v}\right) \quad \text{(Equation 7)}$$

where τ_0 = 800 Pa is the shear yield stress of the matrix, η = 8000 Pa·s is the viscosity of the matrix at room temperature, and $\hat{\mathbf{v}}$ is the unit vector of velocity relative to the surrounding matrix. Moreover, the vector sum of gravity and buoyancy of the CI particle F_i^{gb} is calculated as

$$F_i^{gb} = \frac{\pi d_i^3}{6}(\rho - \rho_0)\mathbf{g} \quad \text{(Equation 8)}$$

Here, ρ and ρ_0 are the density of particles and the matrix, respectively. Because of the yield stress in the matrix, when $|\sum F_i| \leq \frac{19}{8}\pi\tau_0 d_i^2$, particles will not move. Without applying a magnetic field, the sum of gravity and buoyancy $F_i^{gb} \ll \frac{19}{8}\pi\tau_0 d_i^2$ even at 80°C, so there is no particle sedimentation (see Figure S5). The particles move slowly (the moving distance is less than 10 μm in 2 seconds, Figure 7F), so the inertia and

acceleration of the particles are not taken into account. Given the aforemenitoned forces, the equation of motion is established as follows:

$$\sum_{j\neq i}\left(F_{ij}^{m}+F_{ij}^{vdW}+F_{ij}^{r}\right)+F_{i}^{d}+F_{i}^{gb}=0 \qquad \text{(Equation 9)}$$

Equation (9) can be solved using a numerical method and the microstructure in the LMMRP as shown in Figures 7E and 7F. Under a magnetic field, randomly dispersed CI particles gradually tended to chains, and LM droplets were pushed and aggregated around the CI particle chains. The LM droplets in the moving path of CI particles were pushed away by CI particles so that LM droplets were distributed along the direction of the magnetic field. This is equivalent to increasing the volume fraction of LM droplets in the direction of the magnetic field, reducing the distance between LM droplets, and reducing the resistance. For the convenience of observation, Figure 7F shows the evolution of particle microstructure in a 5-μm-thick area. Under the action of push force, the LM droplets in the moving path of CI particles are pushed by CI particles and aggregated around the CI particle chains, forming a conductive channel together with the CI particle chains. When the magnetic field is removed, CI particles tend to be uniform again and the push force on LM droplets is removed. Then, the distance between LM droplets enlarges, and the resistance increases.

Based on the aforementioned analysis, it can be concluded that the CI particles chain and the LM droplets around the chain combine together to form the conductive channel under the magnetic field and further reduces the resistance of LMMRP. The CI-chain structure in the LMMRP acts as a supporting skeleton of the conductive channel. Therefore, the resistance of LMMRP can be changed by adjusting the CI-chain structure. Considering the temperature-dependent viscosity of the polymer, the temperature sensing mechanism of LMMRP based on PU polymer is studied. With increasing the temperature, the distance between the polymer molecules increased and the internal friction decreased. Under an external force, the molecular chain entanglement points were untied, so the shear yield stress and the viscosity of the polymer decreased (Chen, 2013). The viscosity of LMPU with 20% LM also decreased with increasing temperature (see Figure S6). In the low-viscosity matrix, the CI particle chains aggregated into thicker cluster-like structures (see Figure S7). The magnetic potential energy was also derived in the supplementary information (see Figure S8). The magnetic potential energy depends on the particle's position, interaction, and distribution in the matrix, which reflects the evolution of the microstructure. Therefore, the magnetic potential energy U_m is proposed as

$$U_m=\mu_0\sum_i\left[-\boldsymbol{m}_i\cdot\boldsymbol{H}+\sum_{j>i}\frac{1}{4\pi r_{ij}^3}\left(\boldsymbol{m}_i\cdot\boldsymbol{m}_j-3\boldsymbol{m}_i\cdot\boldsymbol{t}\boldsymbol{m}_j\cdot\boldsymbol{t}\right)\right] \qquad \text{(Equation 10)}$$

The results showed that the magnetic potential energy also increased with temperature, which meant that the average moving distance of the CI particles increased and a thicker cluster-like structure is formed. During the formation of denser CI particle chains, more LM droplets would be squeezed to form more conductive channels, thus the resistance decreased. Similarly, the increase of magnetic field could promote the formation of denser CI particle structure and reduce the resistance. When an external force was applied, the LMMRP was compressed and the CI particle chains were broken (Liu et al., 2013b). The dislocation of some CI particles would drive the surrounding LM droplets to move and interrupt the conductive channel (Figure 7D). The fracture of the conductive paths caused a sharp increase in the resistance of the sample. Nonetheless, once the external force was removed, the CI particles reestablished chain-like structures under the magnetic field, and new conductive paths were obtained with the help of the LM droplets. Besides, the PDMS shell wrapped on the surface of the LMMRP facilitated it to return to the original state, increasing the stability and reliability of the LMMRP in force sensing applications.

CONCLUSION

In summary, a shape-deformable flexible multifunctional sensor with a magnetic field "on-off" switch was fabricated by dispersing highly conductive LM droplets and magnetic CI particles into a soft low-cross-linking PU matrix. The LMMRP was insulated at room temperature and became conductive by applying a magnetic field. This composite showed a high sensitive feeding back through electrical resistance to external stimuli such as magnetism, temperature, and force. Because LM droplets worked together with the CI chain-like structures along the direction of the magnetic field to form conductive paths, the electrical resistance of the LMMRP can be significantly reduced. The experimental results demonstrated that the absolute value of the relative resistance variation can reach 95% under the 180-mT magnetic field, indicating the excellent magnetic response characteristics. Moreover, the LMMRP showed a typical temperature-

dependent electric response, and its sensitivity was presented as 1.56%/°C and 0.33%/°C in the 25°C–70°C range, respectively. Especially, the LMMRP had an excellent sensitivity coefficient of 17.7%/N and played an important role in tactile and behavioral perception as a force sensor. The manufacturing process is fast, simple, low cost, and easy to be extended for fabricating large-area sensors. As a result, the LMMRP with multisensing performance and the fast response showed wide application in complex environments and becoming a promising candidate for future artificial electronics.

Limitations of the study

In this study, we assumed that LM droplets would not fuse when pushed by CI particles and the evolution of the particle structure was simulated under this assumption. However, it was difficult for us to directly observe the movement of the LM droplets, so there was no direct evidence that the LM droplets would not fuse. Meanwhile, the deformation of LM droplets was also ignored in the simulation. Technically speaking, the probability of LM droplet fusion will increase with the increase of its moving distance. When the direction of the magnetic field changes frequently, the moving distance of the LM droplet increases. So, the characterization and analysis of the electrical conductivity in different magnetic field directions are warranted for future work.

STAR★METHODS

Detailed methods are provided in the online version of this paper and include the following:

- KEY RESOURCES TABLE
- RESOURCE AVAILABILITY
  - Lead contact
  - Material availability
  - Data and code availability
- METHOD DETAILS
  - Materials
  - Preparation of PU
  - Preparation of LMPU and the LMMRP
  - Fabrication of the LMMRP sensor
  - Characterizations
- QUANTIFICATION AND STATISTICAL ANALYSIS

SUPPLEMENTAL INFORMATION

Supplemental information can be found online at https://doi.org/10.1016/j.isci.2021.102549.

ACKNOWLEDGMENTS

Financial supports from the National Natural Science Foundation of China (Grant No. 11822209, 12072338), the Fundamental Research Funds for the Central Universities (WK2090000007), Joint Fund of USTC-National Synchrotron Radiation Laboratory (KY2090000055), and the Strategic Priority Research Program of the Chinese Academy of Sciences (Grant No. XDB22040502) are gratefully acknowledged.

AUTHOR CONTRIBUTIONS

X.G. and S.X. designed and supervised the whole project. J.X. and H.P. fabricated and characterized the composites, designed and completed the experiments, and analyzed the data. H.P. and L.P. simulated the evolution of internal particle structure. J.X. and S.X. wrote the manuscript. All the authors were actively involved in the discussion, analysis, and revision.

DECLARATION OF INTERESTS

The authors declare no competing interests.

Received: November 30, 2020
Revised: March 24, 2021
Accepted: May 14, 2021
Published: June 25, 2021

REFERENCES

Amjadi, M., Pichitpajongkit, A., Lee, S., Ryu, S., and Park, I. (2014). Highly stretchable and sensitive strain sensor based on silver nanowire-elastomer nanocomposite. ACS Nano *8*, 5154–5163.

Boland, C.S., Khan, U., Ryan, G., Barwich, S., Charifou, R., Harvey, A., Backes, C., Li, Z., Ferreira, M.S., Möbius, M.E., et al. (2016). Sensitive electromechanical sensors using viscoelastic graphene-polymer nanocomposites. Science *354*, 1257–1260.

Chand, S. (2000). Carbon fibers for composites. J. Mater. Sci. *35*, 1303–1313.

Chen, X.M. (2013). The viscosity-temperature and viscosity-shear sensitivity of polymer materials. Polym. Mater. Sci. Eng. *29*, 188–190.

Chen, Y.H., Lu, S.Y., Zhang, S.S., Li, Y., Qu, Z., Chen, Y., Lu, B.W., Wang, X.Y., and Feng, X. (2017). Skin-like biosensor system via electrochemical channels for noninvasive blood glucose monitoring. Sci. Adv. *3*, e1701629.

Chen, T., Shi, Q.F., Zhu, M.L., He, T.Y.Y., Sun, L.N., Yang, L., and Lee, C. (2018). Triboelectric self-powered wearable flexible patch as 3D motion control interface for robotic manipulator. ACS Nano *12*, 11561–11571.

Cheng, S.B., Narang, Y.S., Yang, C.H., Suo, Z.G., and Howe, R.D. (2019). Stick-on large-strain sensors for soft robots. Adv. Mater. Interfaces *6*, 1900985.

Dickey, M.D. (2017). Stretchable and soft electronics using liquid metals. Adv. Mater. *29*, 1606425.

Ding, L., Pei, L., Xuan, S.H., Fan, X.W., Cao, X.F., Wang, Y., and Gong, X.L. (2020). Ultrasensitive multifunctional magnetoresistive strain sensor based on hair-like magnetization-induced pillar forests. Adv. Electron. Mater. *6*, 1900653.

Dresselhaus, M.S., and Dresselhaus, G. (2002). Intercalation compounds of graphite. Adv. Phys. *51*, 1–186.

Gao, Y.J., Yu, L.T., Yeo, J.C., and Lim, C.T. (2020). Flexible hybrid sensors for health monitoring: materials and mechanisms to render wearability. Adv. Mater. *32*, 1902133.

Gheribi, A.E., and Chartrand, P. (2019). Temperature and oxygen adsorption coupling effects upon the surface tension of liquid metals. Sci. Rep. *9*, 7113.

Guo, R., Sun, X.Y., Yuan, B., Wang, H.Z., and Liu, J. (2019). Magnetic liquid metal (Fe-EGaIn) based multifunctional electronics for remote self-healing materials, degradable electronics, and thermal transfer. Adv. Sci. *6*, 1901478.

Ha, M., Lim, S., Cho, S., Lee, Y., Na, S., Baig, C., and Ko, H. (2018). Skin-Inspired hierarchical polymer architectures with gradient stiffness for spacer-Free, ultrathin, and highly sensitive triboelectric sensors. ACS Nano *12*, 3964–3974.

Harada, S., Kanao, K., Yamamoto, Y., Arie, T., Akita, S., and Takei, K. (2014). Fully printed flexible fingerprint-like three-axis tactile and slip force and temperature sensors for artificial skin. ACS Nano *8*, 12851–12857.

Hu, T., Xuan, S.H., Ding, L., and Gong, X.L. (2020). Liquid metal circuit based magnetoresistive strain sensor with discriminating magnetic and mechanical sensitivity. Sens. Actuator B Chem. *314*, 128095.

Jin, L.H., Chortos, A., Lian, F.F., Pop, E., Linder, C., Bao, Z.A., and Cai, W. (2018). Microstructural origin of resistance-strain hysteresis in carbon nanotube thin film conductors. Proc. Natl. Acad. Sci. U S A *115*, 1986–1994.

Kazem, N., Bartlett, M.D., and Majidi, C. (2018). Extreme toughening of soft materials with liquid metal. Adv. Mater. *30*, 1706594.

Kang, J.H., Son, D., Wang, G.J.N., Liu, Y.X., Lopez, J., Kim, Y., Oh, J.Y., Katsumata, T., Mun, J.W., Lee, Y., et al. (2018). Tough and water-insensitive self-healing elastomer for robust electronic skin. Adv. Mater. *30*, 1706846.

Keaveny, E.E., and Maxey, M.R. (2008). Modeling the magnetic interactions between paramagnetic beads in magnetorheological fluids. J. Comput. Phys. *227*, 9554–9571.

Kim, S.L., Choi, K., Tazebay, A., and Yu, C. (2014). Flexible power fabrics made of carbon nanotubes for harvesting thermoelectricity. ACS Nano *8*, 2377–2386.

Klingenberg, D.J., Olk, C.H., Golden, M.A., and Ulicny, J.C. (2010). Effects of nonmagnetic interparticle forces on magnetorheological fluids. J. Phys. Condens. Matter. *22*, 324101.

Kumar, R.R., Gowrisankar, P., Balaprakash, V., Sudha, S., and Manimaran, E.I. (2018). Structural and magnetoresistive properties of electrodeposited thin films for magnetic sensors applications. J. Mater. Sci. Mater. El. *29*, 11591–11597.

Lin, Y.L., Ladd, C., Wang, S.Y., Martin, A., Genzer, J., Khan, S.A., and Dickey, M.D. (2016). Drawing liquid metal wires at room temperature. Extreme Mech. Lett. *7*, 55–63.

Lin, S.Y., Zhong, Y.J., Zhao, X.L., Sawada, T., Li, X.M., Lei, W.H., Wang, M.R., Serizawa, T., and Zhu, H.W. (2018). Synthetic multifunctional graphene composites with reshaping and self-healing features via a facile biomineralization-inspired process. Adv. Mater. *30*, 1803004.

Liu, T.X., Gong, X.L., Xu, Y.G., Xuan, S.H., and Jiang, W.Q. (2013a). Simulation of magneto-induced rearrangeable microstructures of magnetorheological plastomers. Soft Matter *9*, 10069–10080.

Liu, T.X., Xu, Y.G., Gong, X.L., Pang, H.M., and Xuan, S.H. (2013b). Magneto-induced normal stress of magnetorheological plastomer. AIP Adv. *3*, 082122.

Markvicka, E.J., Bartlett, M.D., Huang, X.N., and Majidi, C. (2018). An autonomously electrically self-healing liquid metal-elastomer composite for robust soft-matter robotics and electronics. Nat. Mater. *17*, 618–624.

Melzer, M., Monch, J.I., Makarov, D., Zabila, Y., Bermudez, G.S.C., Karnaushenko, D., Baunack, S., Bahr, F., Yan, C.L., Kaltenbrunner, M., and Schmidt, O.G. (2015). Wearable magnetic field sensors for flexible electronics. Adv. Mater. *27*, 1274–1280.

Moulin, J., Doll, A., Paul, E., Pannetier-Lecoeur, M., Fermon, C., Sergeeva-Chollet, N., and Solignac, A. (2019). Optimizing magnetoresistive sensor signal-to-noise via pinning field tuning. Appl. Phys. Lett. *115*, 122406.

Pang, H.M., Xuan, S.H., Liu, T.X., and Gong, X.L. (2015). Magnetic field dependent electro-conductivity of the graphite doped magnetorheological plastomer. Soft Matter *11*, 6893–6902.

Pang, H.M., Pei, L., Sun, C.L., and Gong, X.L. (2018). Normal stress in magnetorheological polymer gel under large amplitude oscillatory shear. J. Rheol. *62*, 1409–1418.

Park, S., Thangavel, G., Parida, K., Li, S.H., and Lee, P.S. (2019). A stretchable and self-healing energy storage device based on mechanically and electrically restorative liquid-metal particles and carboxylated polyurethane composites. Adv. Mater. *31*, 1805536.

Pei, L., Xuan, S.H., Wu, J., Bai, L.F., and Gong, X.L. (2019). Experiments and simulations on the magnetorheology of magnetic fluid based on Fe3O4 hollow chains. Langmuir *35*, 12158–12167.

Pyo, S., Choi, J., and Kim, J. (2019). A fully transparent, flexible, sensitive, and visible-blind ultraviolet sensor based on carbon nanotube-graphene hybrid. Adv. Electron. Mater. *5*, 1800737.

Qin, Y.Y., Peng, Q.Y., Ding, Y.J., Lin, Z.S., Wang, C.H., Li, Y., Li, J.J., Yuan, Y., He, X.D., and Li, Y.B. (2015). Lightweight, superelastic, and mechanically flexible graphene/polyimide nanocomposite foam for strain sensor application. ACS Nano *9*, 8933–8941.

Ren, L., Zhuang, J.C., Casillas, G., Feng, H.F., Liu, Y.Q., Xu, X., Liu, Y.D., Chen, J., Du, Y., Jiang, L., and Dou, S.X. (2016). Nanodroplets for stretchable superconducting circuits. Adv. Funct. Mater. *26*, 8111–8118.

Ren, L., Xu, X., Du, Y., Kalantar-Zadeh, K., and Dou, S.X. (2020). Liquid metals and their hybrids as stimulus-responsive smart materials. Mater. Today *34*, 92–114.

Tang, S.Y., Joshipura, I.D., Lin, Y.L., Kalantar-Zadeh, K., Mitchell, A., Khoshmanesh, K., and Dickey, M.D. (2016). Liquid-metal microdroplets formed dynamically with electrical control of size and rate. Adv. Mater. *28*, 604–609.

Wang, Z.G., Wang, X.J., Li, M.H., Gao, Y., Hu, Z.Q., Nan, T.X., Liang, X.F., Chen, H.H., Yang, J., Cash, S., and Sun, N.X. (2016). Highly sensitive flexible magnetic sensor based on anisotropic magnetoresistance effect. Adv. Mater. *28*, 9370–9377.

Wang, J.X., Cai, G.F., Li, S.H., Gao, D.C., Xiong, J.Q., and Lee, P.S. (2018). Printable superelastic conductors with extreme stretchability and

robust cycling endurance enabled by liquid-metal particles. Adv. Mater. *30*, 1706157.

Wang, Y.M., Xu, Z., Lovrak, M., le Sage, V.A.A., Zhang, K., Guo, X.H., Eelkema, R., Mendes, E., and van Esch, J.H. (2020). Biomimetic strain-stiffening self-assembled hydrogels. Angew. Chem. Int. Ed. Engl. *59*, 4830–4834.

Xiong, H., Zhang, L.J., Wu, Q., Zhang, H., Peng, Y., Zhao, L.J., Huang, G.S., and Wu, J.R. (2020). A strain-adaptive, self-healing, breathable and perceptive bottle-brush material inspired by skin. J. Mater. Chem. A *8*, 24645–24654.

Xu, Y.G., Gong, X.L., Xuan, S.H., Zhang, W., and Fan, Y.C. (2011). A high-performance magnetorheological material: preparation, characterization and magnetic-mechanic coupling properties. Soft Matter *7*, 5246–5254.

Xu, Y.G., Gong, X.L., Xuan, S.H., Li, X.F., Qin, L.J., and Jiang, W.Q. (2012). Creep and recovery behaviors of magnetorheological plastomer and its magnetic-dependent properties. Soft Matter *8*, 8483–8492.

Xu, Y.G., Gong, X.L., Liu, T.X., and Xuan, S.H. (2013). Magneto-induced microstructure characterization of magnetorheological plastomers using impedance spectroscopy. Soft Matter *9*, 7701–7709.

Xu, J.Q., Pei, L., Li, J., Pang, H.M., Li, Z.Y., Li, B.S., Xuan, S.H., and Gong, X.L. (2019). Flexible, self-powered, magnetism/pressure dual-mode sensor based on magnetorheological plastomer. Compos. Sci. Technol. *183*, 107820.

Yao, S.S., and Zhu, Y. (2014). Wearable multifunctional sensors using printed stretchable conductors made of silver nanowires. Nanoscale *6*, 2345–2352.

Yuan, F., Wang, S., Zhang, S.S., Wang, Y., Xuan, S.H., and Gong, X.L. (2019). A flexible viscoelastic coupling cable with self-adapted electrical properties and anti-impact performance toward shapeable electronic devices. J. Mater. Chem. C *7*, 8412–8422.

Yun, G.L., Tang, S.Y., Sun, S.S., Yuan, D., Zhao, Q.B., Deng, L., Yan, S., Du, H.P., Dickey, M.D., and Li, W.H. (2019). Liquid metal-filled magnetorheological elastomer with positive piezoconductivity. Nat. Commun. *10*, 1300.

Yun, G.L., Tang, S.Y., Zhao, Q.B., Zhang, Y.X., Lu, H.D., Yuan, D., Sun, S.S., Deng, L., Dickey, M.D., and Li, W.H. (2020). Liquid metal composites with anisotropic and unconventional piezoconductivity. Matter *3*, 824–841.

Zhang, S.S., Wang, S., Wang, Y.P., Fan, X.W., Ding, L., Xuan, S.H., and Gong, X.L. (2018). Conductive shear thickening gel/polyurethane sponge: a flexible human motion detection sensor with excellent safeguarding performance. Compo. A Appl. Sci. Manufact. *112*, 197–206.

Zhang, Q., Du, Y., Sun, Y.Y., Zhuo, K., Ji, J.L., Yuan, Z.Y., Zhang, W.D., and Sang, S.B. (2019). A flexible magnetic field sensor based on AgNWs & MNs-PDMS. Nanoscale Res. Lett. *14*, 27.

Zhao, C.Y., Wang, Y.P., Cao, S.S., Xuan, S.H., Jiang, W.Q., and Gong, X.L. (2019). Conductive shear thickening gel/Kevlar wearable fabrics: a flexible body armor with mechano-electric coupling ballistic performance. Compo. Sci. Techn. *182*, 107782.

STAR★METHODS

KEY RESOURCES TABLE

REAGENT or RESOURCE	SOURCE	IDENTIFIER
Chemicals, peptides, and recombinant proteins		
Polypropylene glycol	Sinopharm Chemical Reagent Co. Ltd.	Cat#40812; CAS: 25322-69-4
Tolylene diisocyanate	Sigma-Aldrich	Cat#216836; CAS: 584-84-9
Diethylene glycol	Sinopharm Chemical Reagent Co. Ltd.	Cat#30058718; CAS: 111-46-6
Software and algorithms		
Microsoft Visual Studio 2008	Microsoft Corporation	https://visualstudio.microsoft.com/

RESOURCE AVAILABILITY

Lead contact

Further information and requests for resources should be directed to and will be fulfilled by the lead contact, Shouhu Xuan (xuansh@ustc.edu.cn).

Material availability

The study did not generate any unique reagents.

Data and code availability

No new code is generated and all original data are available from the authors upon request.

METHOD DETAILS

Materials

The raw materials for the synthesis of polyurethane (PU) included polypropylene glycol (PPG-1000, Sinopharm Chemical Reagent Co. Ltd., China), tolylene diisocyanate (TDI, technical grade, 80%, Sigma-Aldrich, USA), and diethylene glycol (DEG, Sinopharm Chemical Reagent Co. Ltd., Shanghai, China). PU is the matrix of the liquid-metal (LM)-filled magnetorheological plastomer (LMMRP). The carbonyl iron (CI) particles with an average diameter of 7 μm were purchased from BASF Aktiengesellschaft, Germany. The LM composed of 75% Ga and 25% In was purchased from Yongcheng Hardware Machinery Manufacturing Co., Ltd. Dongguan City, Guangdong Province. The PDMS precursor and the curing agent (Sylgard 184) were purchased from Dow Corning GmbH, USA.

Preparation of PU

First, TDI and PPG were added to a flask at a ratio of 3: 1 and stirred continuously at 80°C for 2 h. Their weights were calculated using the following formula:

$$\frac{m_{TDI} \Big/ 174 \cdot mol^{-1}}{m_{PPG} \Big/ 1000 \cdot mol^{-1}} = 3 \qquad \text{(Equation 11)}$$

where m_{TDI} and m_{PPG} indicate the weights of TDI and PPG, and the numbers are the molecular weights of the compounds. Then, the reactor was cooled to 40°C. Second, DEG was added to the flask and the temperature was set to be 60°C. After 30 min, the homemade PU matrix was synthesized. The weight of DEG was calculated by the following formula:

$$\frac{m_{TDI} \Big/ 174 \cdot mol^{-1}}{\frac{m_{PPG}}{1000} \cdot mol^{-1} + \frac{m_{DEG}}{106} \cdot mol^{-1}} = 1.1 \qquad \text{(Equation 12)}$$

Preparation of LMPU and the LMMRP

A total amount of 1 mol·L^{-1} NaOH was used to remove the LM surface oxide layer. The NaOH was removed before adding to PU. The NaOH-treated LM was added to the heated PU (the heating temperature was 60°C) and stirred vigorously by hand until it was uniformly dispersed in the matrix. Then, the LMPU was prepared. In addition, the LMMRP was made by adding the CI particles to the as-prepared LMPU.

Fabrication of the LMMRP sensor

A PDMS base (30 mm×30 mm×2 mm) with a circular hole (the diameter was 20 mm and the depth was 1 mm) was prepared by a mold filling method. The top and bottom surfaces of the LMMRP were closely attached to two copper foils, which were placed in the hole. Besides, a copper wire was connected to each copper foil to transmit electrical characteristics. Finally, the PDMS was covered on the upper layer for sealing.

Characterizations

The morphologies of the LMPU and the LMMRP were imaged by a scanning electron microscope (Gemini 500, Carl Zeiss Jena, Germany). The Chamber SE Detector was used and the accelerating voltage was set as 20 kV. The rheological properties and magnetic/thermal/mechanical sensing properties of the LMMRP were tested by a commercial rheometer (Physica MCR301, Anton Paar Co., Austria) equipped with a magneto-controllable accessory MRD180 and temperature control module. A ModuLab material test system (Solartron analytical, AMETEK advanced measurement technology, Inc., United Kingdom) was used to measure and analyze the electrical properties (the DC voltage was 4.0 V). All samples are treated under a 780-mT magnetic field for more than 300 s as a preconfiguration process before testing. After the preconfiguration process, the particle structure tends to be stable. All digital photos were taken by a digital camera (D1700, Nikon).

QUANTIFICATION AND STATISTICAL ANALYSIS

The data in Figures 1D, 1F, 2E, 2H, 4B, 4C, 4G, and 6B are the average results of three tests, which are stated in the figure legends. The CI particle size distribution is referred to the literature source (Liu et al., 2013a), which can be found in the results and discussion.